Article

A Convenient In Situ Preparation of Cu₂ZnSnS₄–Anatase Hybrid Nanocomposite for Photocatalysis/Photoelectrochemical Water-Splitting Hydrogen Production

Ke-Xian Li [1,2,3], Cai-Hong Li [1,3,4], Hao-Yan Shi [1,3], Rui Chen [1,3], Ao-Sheng She [1,3], Yang Yang [1,2,3], Xia Jiang [1,3], Yan-Xin Chen [1,2,3,*] and Can-Zhong Lu [1,2,3,*]

[1] State Key Laboratory of Structural Chemistry, Fujian Science & Technology Innovation Laboratory for Optoelectronic Information of China, Fujian Institute of Research on the Structure of Matter, Chinese Academy of Sciences, Fuzhou 350108, China; xmlikexian@fjirsm.ac.cn (K.-X.L.); xmlicaihong@fjirsm.ac.cn (C.-H.L.); xmshihaoyan@fjirsm.ac.cn (H.-Y.S.); xmchenrui@fjirsm.ac.cn (R.C.); xmsheaosheng@fjirsm.ac.cn (A.-S.S.); xmyangyang@fjirsm.ac.cn (Y.Y.); xmjiangxia@fjirsm.ac.cn (X.J.)

[2] College of Chemistry and Materials Science, Fujian Normal University, Fuzhou 350108, China

[3] Xiamen Key Laboratory of Rare Earth Photoelectric Functional Materials, Xiamen Institute of Rare-Earth Materials, Haixi Institutes, Chinese Academy of Sciences, Xiamen 361021, China

[4] College of Chemistry, Fuzhou University, Fuzhou 350116, China

* Correspondence: yanxinchen@fjirsm.ac.cn (Y.-X.C.); czlu@fjirsm.ac.cn (C.-Z.L.)

Abstract: This study details the rational design and synthesis of Cu₂ZnSnS₄ (CZTS)-doped anatase (A) heterostructures, utilizing earth-abundant elements to enhance the efficiency of solar-driven water splitting. A one-step hydrothermal method was employed to fabricate a series of CZTS–A heterojunctions. As the concentration of titanium dioxide (TiO₂) varied, the morphology of CZTS shifted from floral patterns to sheet-like structures. The resulting CZTS–A heterostructures underwent comprehensive characterization through photoelectrochemical response assessments, optical measurements, and electrochemical impedance spectroscopy analyses. Detailed photoelectrochemical (PEC) investigations demonstrated notable enhancements in photocurrent density and incident photon-to-electron conversion efficiency (IPCE). Compared to pure anatase electrodes, the optimized CZTS–A heterostructures exhibited a seven-fold increase in photocurrent density and reached a hydrogen production efficiency of 1.1%. Additionally, the maximum H₂ production rate from these heterostructures was 11-times greater than that of pure anatase and 250-times higher than the original CZTS after 2 h of irradiation. These results underscore the enhanced PEC performance of CZTS–A heterostructures, highlighting their potential as highly efficient materials for solar water splitting. Integrating Cu₂ZnSnS₄ nanoparticles (NPs) within TiO₂ (anatase) heterostructures implied new avenues for developing earth-abundant and cost-effective photocatalytic systems for renewable energy applications.

Keywords: copper-based sulfides; heterojunction; photocatalytic H₂ generation; Cu₂ZnSnS₄–anatase nanocomposite

1. Introduction

The quest for clean energy solutions has become imperative to address the escalating environmental pollution and energy shortages. The rampant release of nitrogen, sulfur oxides, and other emissions from fossil fuel combustion, including greenhouse gas CO₂, has significantly tainted our environment. Considering this, hydrogen energy has garnered substantial interest in recent years due to its environmental sustainability, high energy density by weight (approximately 143 MJ/kg calorific value), and potential for recyclability [1,2]. The concept of photocatalytic water splitting, a promising avenue for green hydrogen production, was first demonstrated by Fujishima and Honda in 1972. This process efficiently converts sunlight into hydrogen, making it an ideal technology

for sustainable energy production [3]. However, effective photocatalysts for the hydrogen evolution reaction (HER) must satisfy several requirements: (i) the photo-excited valence band (VB) holes must have an oxidation-reduction potential that is sufficiently positive to serve as electron acceptors, and (ii) the photo-excited electrons in the conduction band (CB) should exhibit an oxidation-reduction potential that is more negative than that of the H_2/reduction product redox potential [4]. Given these prerequisites, photocatalysts that feature optimal band gaps (ranging from 1.45 to 3.3 eV) and can harness approximately 43% of the solar spectrum are known to exhibit robust redox capabilities essential for photocatalytic HER. Therefore, identifying suitable semiconductor materials has become a critical endeavor [5,6].

In the field of semiconductor photocatalysis, exploiting semiconductor materials like g-C_3N_4, CdS, and Cu-based sulfides for photocatalytic water splitting has been recognized as a promising avenue for hydrogen production, addressing the global energy challenge [6]. TiO_2 has emerged as a promising photocatalyst, celebrated for its exceptional stability and resistance to photo and chemical corrosion during reactions. Its suitable band gap allows for excitation by ultraviolet light, while its high catalytic activity and photo-generated charge carriers with a strong redox capacity have garnered significant scientific interest. This surge in attention traces back to the groundbreaking work by Fujishima and Honda, who first reported on photoelectrochemical (PEC) water splitting using TiO_2 electrodes [4,7–11]. However, the practical application of TiO_2 is somewhat constrained by its relatively large band gap (3.0~3.2 eV) and the rapid recombination rate of light-generated electron–hole pairs, limiting its efficient utilization of visible light [7,12]. Various strategies have been explored to overcome these limitations, including elemental doping, surface modification, and semiconductor coupling with materials like CdS and CeO [1,12,13]. It has been discovered that anchoring elements and forming heterojunctions with p-type semiconductors can effectively narrow the band gap and broaden the spectral response range of n-type TiO_2. These methods serve as cost-effective and performance-enhancing strategies to amplify TiO_2's photocatalytic efficiency. Specifically, the transfer of interfacial electrons from the n-type to the p-type region plays a pivotal role in generating photoluminescent electron–hole pairs, promoting their separation, and prolonging their lifetime [4,11,14,15].

The quaternary semiconductor Cu_2ZnSnS_4 (CZTS) has emerged as a standout non-toxic absorber material in the quest for environmentally friendly and cost-effective photocatalysts. Owing to its direct band gap of 1.50 eV, high absorption coefficient (~10^4 cm^{-1}), substantial crustal abundance (Cu: 55 ppm, Zn: 80~100 ppm, Sn: 2.2 ppm), and robust stability, CZTS has become a promising candidate material [2,8,14,16–22]. Its appealing properties have led to its widespread adoption in heterojunction coupling applications. Historically, Cu-sulfur-based materials like Cu(In, Ga) (S, Se)$_2$ (CIGS) and Cu_2ZnSnS_4 (CZTS) have undergone extensive investigation. Specifically, CZTS-based p-n heterojunction photocatalysts have been explored—including configurations such as CZTS/ZnO, CZTS/ SnO$_2$, CZTS/WO, and CZTS/La$_2$TiO$_7$, which have been successfully utilized for the degradation of organic pollutants and CO_2 reduction. These studies underscore CZTS's efficacy as a suitable co-catalyst in p-n heterojunction photocatalytic applications [1,4,7,12,13,21].

CZTS has emerged as a highly effective metal semiconductor for producing thin film photo-cathodes in PEC (photoelectrochemical) water-splitting cells, focusing on catalyzing the hydrogen evolution reaction (HER). Sami and his team utilized pulsed laser deposition (PLD) techniques to fabricate Cu_2ZnSnS_4 (CZTS) films with varying thicknesses on soda-lime glass substrates. Their investigation revealed that larger CZTS particles could hinder light propagation, thus impacting the film's ability to absorb photons effectively. Notably, a CZTS photocatalyst with a thickness of 242 nm exhibited the highest photocatalytic performance among all of the samples tested [23]. These findings illustrate how manipulating nanocrystal size and other synthesis parameters can finely adjust the material's physical and optical characteristics. CZTS displays enhanced photocatalytic activity at the nanoscale level compared to its bulk form, making it an excellent choice for applications such as counter electrodes and photocathodes in solar cells [24]. Jiang and his team also reported

significant progress by employing a spray-sulfurization method for CZTS absorber layers, combined with a sandwich-structured buffer layer of $HfO_2/CdS/HfO_2$. This configuration achieved a remarkable photocurrent density (Jph) of 28 mA cm^{-2} at 0 V_{RHE} (voltage vs. reversible hydrogen electrode) and an onset potential (Von) of 0.72 V_{RHE}, resulting in an impressive hydrogen conversion efficiency of 7.27% [25]. In a related study, Liang and his colleagues developed CZTSSe ($Cu_2ZnSn(S,Se)_4$) light-absorbing films characterized by high crystallinity and a dense crystal structure. They constructed a $Mo/CZTSSe/CdS/TiO_2/Pt$ photocathode, focusing on optimizing the thickness of CZTSSe to minimize defect density and maximize built-in voltage. This optimized configuration significantly reduced defect-assisted recombination, thereby improving charge transfer and separation efficiencies. Notably, the half-cell solar hydrogen production efficiency of the optimized CZTSSe photocathode reached 6.47% [26,27]. These accomplishments underscore the promising potential of modified CZTS materials for efficient solar hydrogen production, highlighting the significant role CZTS-based materials could play in enhancing photocathode performance for solar-powered hydrogen generation.

The above study demonstrates how p-n junctions can be effectively tuned by adjusting the composition to modulate band gap energy levels, creating a band structure optimized for water reduction, and achieving a relatively high photocatalytic and PEC performance [14,28]. Motivated by the remarkable properties of CZTS, there is anticipation that p-n heterostructures comprising CZTS–TiO_2 nanocomposite photocatalysts could serve as viable, precious-metal-free, and environmentally friendly catalysts in photocatalytic hydrogen evolution reactions.

This paper presents a simple in situ method for synthesizing a CZTS–anatase hybrid nanocomposite. This approach reduces the band gap of titanium dioxide and enhances the concentration of photo-generated charge carriers, significantly improving the photocatalytic performance for hydrogen evolution. Extensive studies were conducted on the microstructure and photoactivity of the CZTS–anatase composite materials. The results indicate that the photocatalytic activity of the CZTS–anatase heterojunction-structured nanocomposite is enhanced by the formation of p-n heterojunctions with CZTS acting as a co-catalyst, surpassing the performance of both pristine CZTS and anatase alone. Furthermore, this cost-effective, robust, and versatile method allows for synthesizing multiphase/TiO_2 heterojunction semiconductors in a relatively short time and at lower temperatures, offering a promising avenue for developing advanced photocatalytic materials.

2. Results and Discussion

2.1. Structure and Morphology

The crystalline phases and structural characteristics of the synthesized CZTS NPs, anatase titanium dioxide synthesized by TOBT, and hybrid CZTS–A_X (X = 1, 3, 5, 7, 9) nanocomposites were analyzed using X-ray diffraction (XRD). As depicted in Figure 1, the X-ray diffraction spectra present characteristic peaks at 2θ = 28.5°, 47.3°, and 56.1°, which correspond to the (112), (220), and (312) facets of Kesterite CZTS (JCPDS 26-0575) [17,29–31], respectively. The lattice constants derived from the XRD peaks are a = 0.542 nm and c = 1.093 nm. The XRD spectra of the CZTS–Ax (X = 1, 3, 5, 7, 9) nanocomposites prepared by TBOT are at 2θ = 25.3°, 37.8°, 48.0°, 53.9°, 55.0°, 62.7°, and 68.7°, respectively, corresponding to the (101), (004), (200), (105), (211), (204), and (116) planes, which could be associated with anatase TiO_2 (JCPDS 21-1272). All the mixed CZTS–Ax samples exhibited characteristic peaks of anatase titanium dioxide, and potassium feldspar peaks are also observed at 2θ = 28.4°, 47.3°, and 56.1°, indicating the successful hybridization of the two. With the increase in the addition of anatase (TBOT was added to the precursor solution in varying proportions) to 9 mL, the XRD apex of anatase at 2θ = 25.3°, 48.0° is more distinct, suggesting the successful hybridization of anatase and potassium feldspar CZTS composites. By observing the XRD spectra and diffraction patterns, it can be discerned that the sharpness of the peaks in the patterns has decreased, indicating that they are nanocrystalline, and the level of crystallinity decreases accompanied by the addition of TBOT. In the

synthesis process exemplified by CZTS–A$_5$, the molar ratio of CZTS to TiO$_2$ was maintained at 1:3, which resulted in the suppression of CZTS peaks due to the addition of titanium dioxide. The typical grain size of each sample was calculated using the Debye–Scherrer equation (see Equation (1)) [30].

$$d = \frac{0.9 \times \lambda}{\beta \times cos\theta} \tag{1}$$

Based on the comprehensive XRD spectrum analysis results, it can be inferred that the grain size of the rutile TiO$_2$ and CZTS composite material slightly decreases, and the crystallinity decreases. These changes may have a significant impact on the photocatalytic performance of the material. The reduced grain size may increase the surface area of the material, increase the density of active sites in photocatalytic reactions, and thus promote the generation and separation of photo-generated electron–hole pairs. However, the decrease in crystallinity may lead to an increase in lattice defects, affecting the efficiency of electron transfer and photocatalytic reactions. Therefore, the grain size and crystallinity changes in rutile TiO$_2$ and CZTS composite materials may jointly affect their photocatalytic performance, and further experimental verification and in-depth research are needed to evaluate their effects comprehensively.
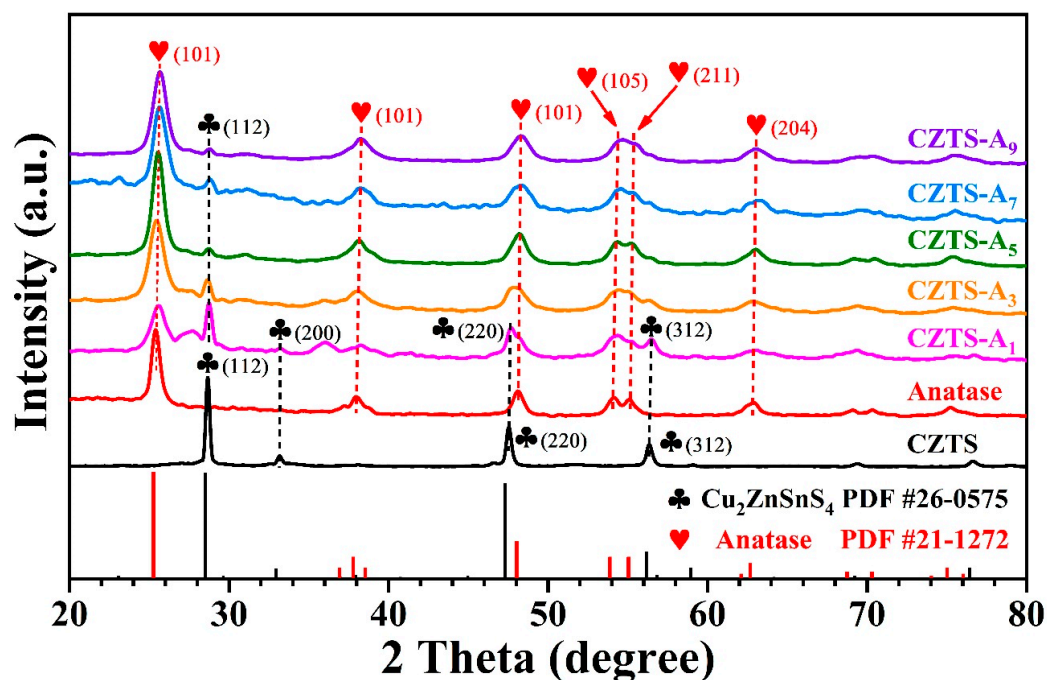

Figure 1. XRD patterns of the Cu$_2$SnZnS$_4$ (CZTS), the anatase TiO$_2$, and the CZTS–A$_X$ (X = 1, 3, 5, 7, 9).

The morphology and microstructure characteristics of composite materials were extensively studied using scanning electron microscopy (SEM) and high-resolution transmission electron microscopy (HR-TEM). Figure 2 shows the SEM and EDS mapping images of the anatase materials (Figure 2a–d), CZTS materials (Figure 2e–k), and CZTS–A$_5$ nanocomposite materials (Figure 2l–u), which were obtained by hydrothermal methods. Figure 2a shows that the anatase material exhibits a typical spherical particulate structure, Figure 2c,d shows that the Ti and O elements are uniformly distributed in the EDS, Figure 2e shows that the CZTS is assembled in nanosheets, and the EDS spectra (Figure 2g–j) show a uniform distribution of the elements. In addition, the SEM images of the CZTS nanoparticles, obtained from the precursor without surfactants and the tetra-n-butyl titanate (TBOT), reveal a relatively homogenous distribution of CZTS nanoparticles exhibiting a flower-like structure and nanosheet morphology (refer to Figure 2l–n). However, introducing TBOT leads to dense agglomerations, presumably due to increased surface energy, which promotes compact clustering and diminishes crystallinity. A comparative analysis of Figure 2

with Figures S1 and S2 indicates that all hybrid composites display similar morphologies, featuring Kesterite CZTS and TiO$_2$ (anatase) heterojunction structures.
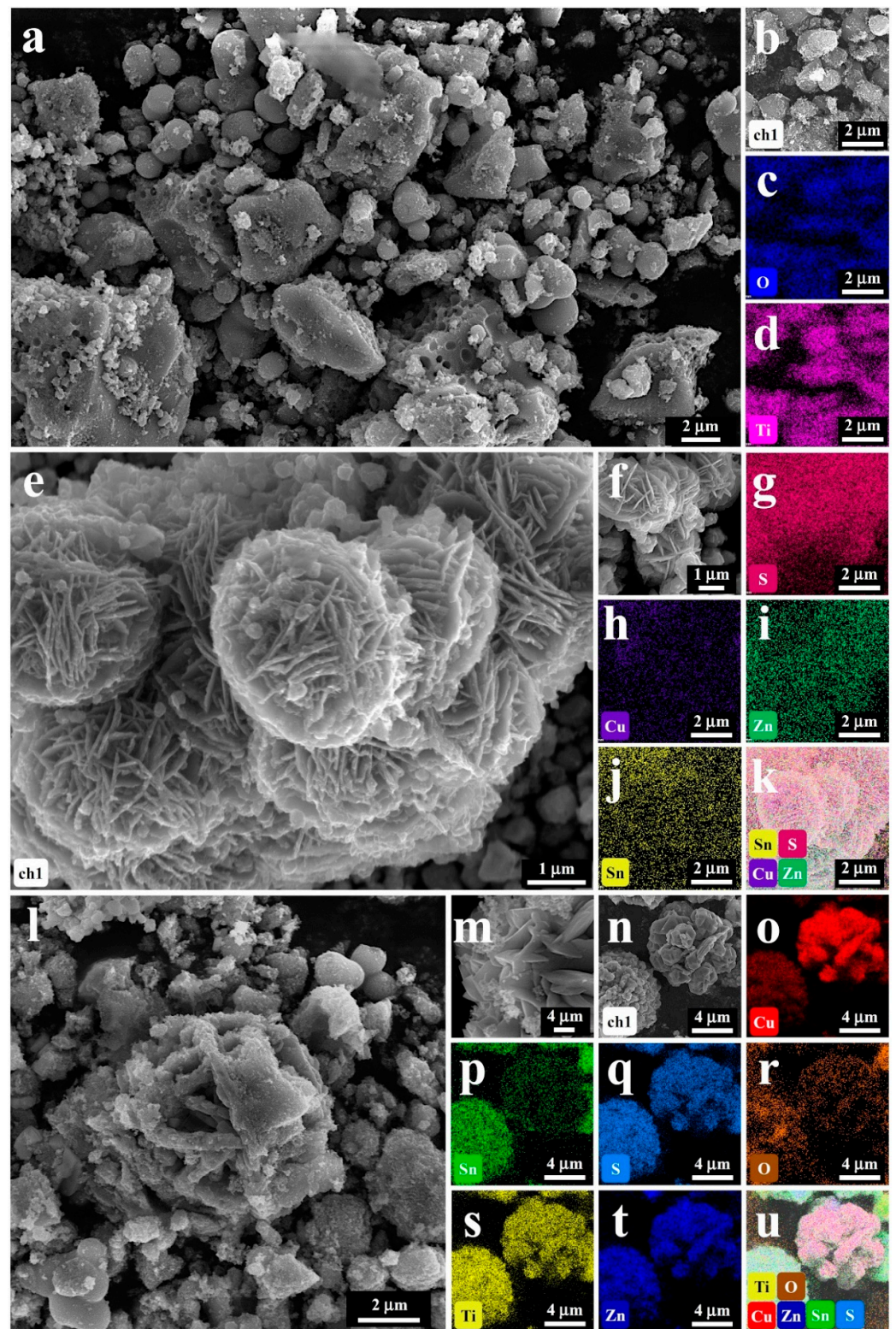

Figure 2. SEM and EDS-mapping images (Cu, Zn, S, Sn, O, and Ti) of (**a–d**) anatase; (**e–k**) CZTS; (**l–u**) CZTS–A$_5$.

Nonetheless, incorporating TBOT initiates a gradual transition towards larger TiO$_2$ particle-like morphologies, accompanied by a reduction in nanosheet forms. As the TiO$_2$

concentration escalates, the nanosheet particles progressively evolve into an average particle size ranging from 20 to 40 nm. The XRD results indicate that the average grain size of the hybrid nanocomposite materials (40 nm) is significantly smaller than depicted in the SEM images. This suggests that larger particles are possible because of TiO_2 (anatase) accumulation and the aggregation of small CZTS nanograins on the TiO_2 (anatase) surface. Furthermore, the identification cannot distinguish TiO_2 (anatase) and CZTS nanocrystals.

An EDS spectrum element analysis was performed to further analyze the elemental distribution of the CZTS–A_5 nanocomposite material. The EDS spectrum analysis in Figure 2c–h indicates that the identified elements in the composite material mainly consist of (Ti), (O), (Cu), (Zn), (Sn), and (S). The elemental mapping indicates that the Cu, Zn, Sn, and S elements are uniformly clustered together, while the Ti and O elements are encapsulated on the periphery, providing data for the successful synthesis and hybridization of the TiO_2 (anatase) and CZTS composite materials.

Additionally, as shown in Figure 3a,c, high-resolution images generated from TEM analysis illustrate the hydrothermally synthesized CZTS NPs and the heterogeneous hybrid CZTS–A_5 nanocomposite materials. The images reveal that the CZTS sample consists of nanosheet structures with an average diameter of approximately 40 nm.
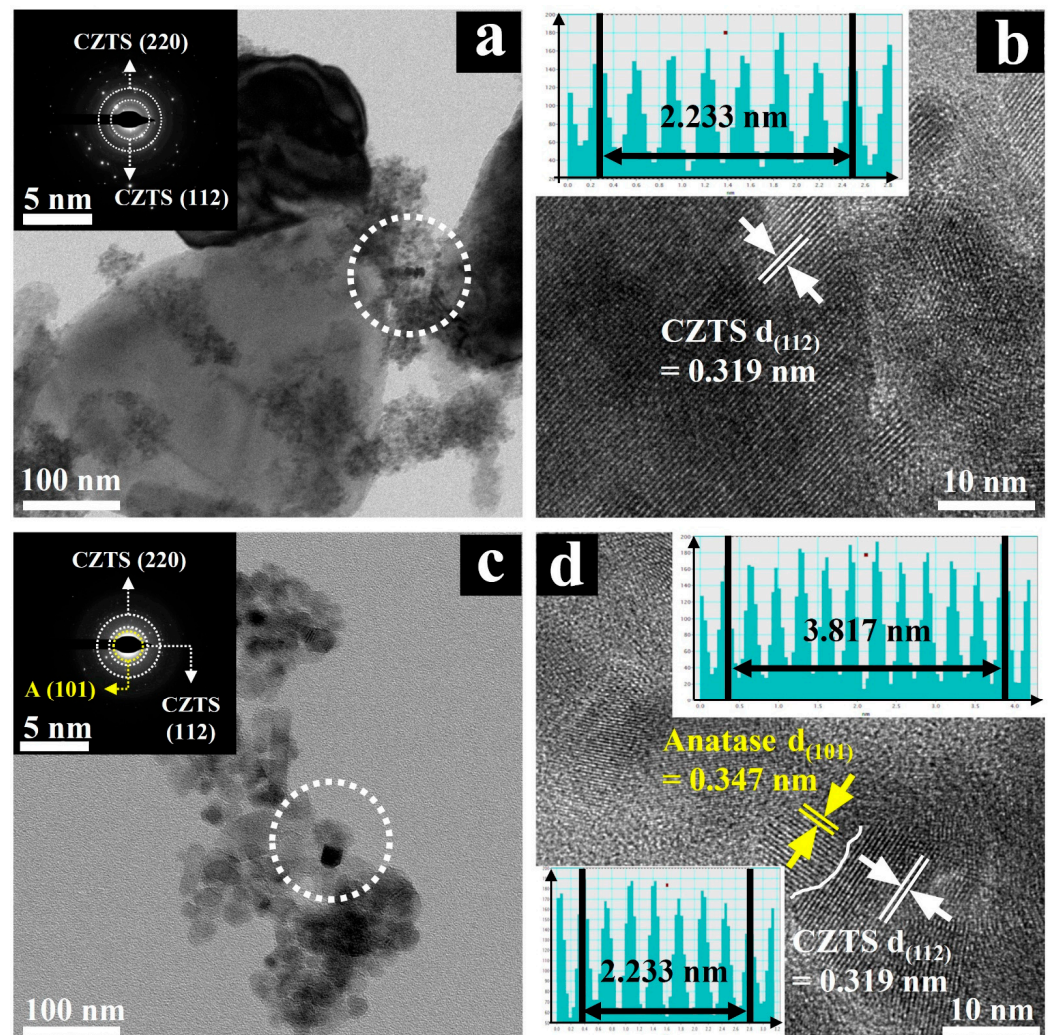

Figure 3. The TEM/HRTEM images and the corresponding SAED patterns of (**a**,**b**) CZTS and (**c**,**d**) CZTS–A_5.

Furthermore, the selected area electron diffraction (SAED) image, which was recorded from the dotted circle area of Figure 3a, shows that the synthesized CZTS NPs exhibit

polycrystalline properties, featuring distinctive rings corresponding to CZTS (112)/(220) planes, consistent with XRD results. In addition, the lattice fringe and IFFT image of CZTS, as shown in Figure 3b, clearly indicate a lattice spacing of 0.319 nm related to the CZTS (112) crystal plane, which is in good agreement with the literature [14,18,32,33].

The SAED pattern of the CZTS–A_5 sample, recorded from the dotted circle area in Figure 3c, shows featuring distinctive rings corresponding to CZTS (220)/(112) and anatase (101) planes. A representative lattice fringe and IFFT image of the CZTS–A_5 sample are demonstrated in Figure 3d. The lattice spacing of 0.342 nm is consistent with the (101) plane of TiO_2 (anatase), and 0.319 nm aligns with the (112) plane of kesterite CZTS. The HRTEM image of CZTS–A_5 exhibits the uniform distribution of nanoscale TiO_2 nanoparticles on the sheet-like CZTS structure, with a complete interface contact between TiO_2 (anatase) and CZTS evident (white curve), forming effective embedding. Which further confirms the formation of heterogeneous structures.

2.2. XPS Characterization

Advanced X-ray photoelectron spectroscopy (XPS) was used to analyze the CZTS–A_X nanocomposites to determine the composition of the major elements in the CZTS–A_X (X = 5) nanocomposites as well as their electronic states (Figures 4 and S3). All elemental analytical energy spectra were calibrated concerning the binding energy (BE) of the 284.6 eV (C 1s) peak for this analysis. As shown in Figure 4a, by analyzing the valence band spectra of each element, in the Cu 2p spectrum, the two apexes of CZTS were clustered at 932 eV (Cu $2p_{1/2}$) and 951.9 eV (Cu $2p_{3/2}$), showing a peak distinction of 19.9 eV, which corresponds to Cu 2p, while the binding energies of Cu 2p were concentrated in CZTS–A_X at 932.4 eV (Cu $2p_{1/2}$) and 952.6 eV (Cu $2p_{3/2}$), showing a binding energy difference of 20.2 eV. These results confirm the presence of Cu^+ in both cases. Two accompanying satellite peaks were observed at binding energies of 934.0 eV, 954.1 eV, and 943.4 eV. These peaks indicate the presence of Cu^{2+} valence states in the sample due to an increase in copper content, which may lead to adjustments in the electronic structure of the material, thereby affecting its photocatalytic performance. Specifically, the presence of Cu^{2+} may alter the material's light absorption characteristics, electron transfer performance, and distribution of surface active sites, thereby affecting the rate and efficiency of photocatalytic reactions [14,32–34].

XPS spectra also revealed the Zn 2p binding energy peaks, with three distinct peaks observed in Figure 4b. In CZTS, two strong peaks are located around 1045.0 eV (Zn $2p_{1/2}$) and 1021.8 eV (Zn $2p_{3/2}$), separated by 23.2 eV. In CZTS–A_5, the intense peak is concentrated at 1045.3 eV (Zn $2p_{1/2}$) and 1022.1 eV (Zn $2p_{3/2}$), maintaining the same splitting value of 23.2 eV, indicating the presence of the Zn^{2+} oxidation state [32,33,35]. The appearance of Zn^{2+} may be related to the conductivity and light absorption characteristics of the material. In Figure 4c, two satellite peaks of the Sn 3d binding energy peak appear. In CZTS, the Sn binding energy is concentrated near 495.0 eV (Sn $3d_{3/2}$) and 486.6 eV (Sn $2d_{5/2}$), while in CZTS–A_5, it is concentrated at 486.8 eV (Sn $2d_{5/2}$) and 495.2 eV (Sn $3d_{3/2}$). The regular splitting is measured to be 8.6 eV, confirming the oxidation state of Sn^{4+}. The presence of Sn^{4+} may alter the charge transfer characteristics and surface reactivity of the material, thereby affecting its photocatalytic performance. In Figure 4d, the S 2p shows two distinct peaks with a binding energy disparity of 1.1 eV, positioned at 162.9 eV (S $2p_{1/2}$) and 161.8 eV (S $2p_{3/2}$). This range is consistent with the reported binding energy of sulfur in sulfides, indicating the oxidation state of sulfides. The binding energy shift of the S 2p peak in CZTS is lower, indicating the electron enrichment of sulfur, suggesting the presence of sulfur vacancies [32,36,37]. These phenomena may affect the surface chemical reactions and photo-generated charge separation processes of materials, affecting their photocatalytic performance. The XPS spectra in Figure 4e also show the Ti 2p binding energy peak. In CZTS–anatase, the Ti binding energies of Ti $2p_{1/2}$ and Ti $2p_{3/2}$ are mainly located at 464.4 eV and 458.7 eV, individually, indicating the presence of the Ti^{4+} oxidation state [12,33]. The absence of the Ti peak in CZTS confirms the successful doping of TiO_2. In addition, Figure 4f shows an O 1s peak centered at 531.6 eV in CZTS, with its intensity

decreasing with the addition of TiO_2. In CZTS–A_5, the characteristic O 1s peak shifts to 529.9 eV, corresponding to fully oxidized lattice oxygen. The intensity changes, and peak position shifts of the O1s peak also indicate changes in the oxidation state of the material, which may affect the surface chemical activity of the material and the rate of photocatalytic reactions. XPS measurements confirm that all the corresponding peaks in the CZTS–A_5 nanocomposites are highly consistent with the reported values, indicating no substantial differences regarding the electronic configuration of the respective materials [14,33].
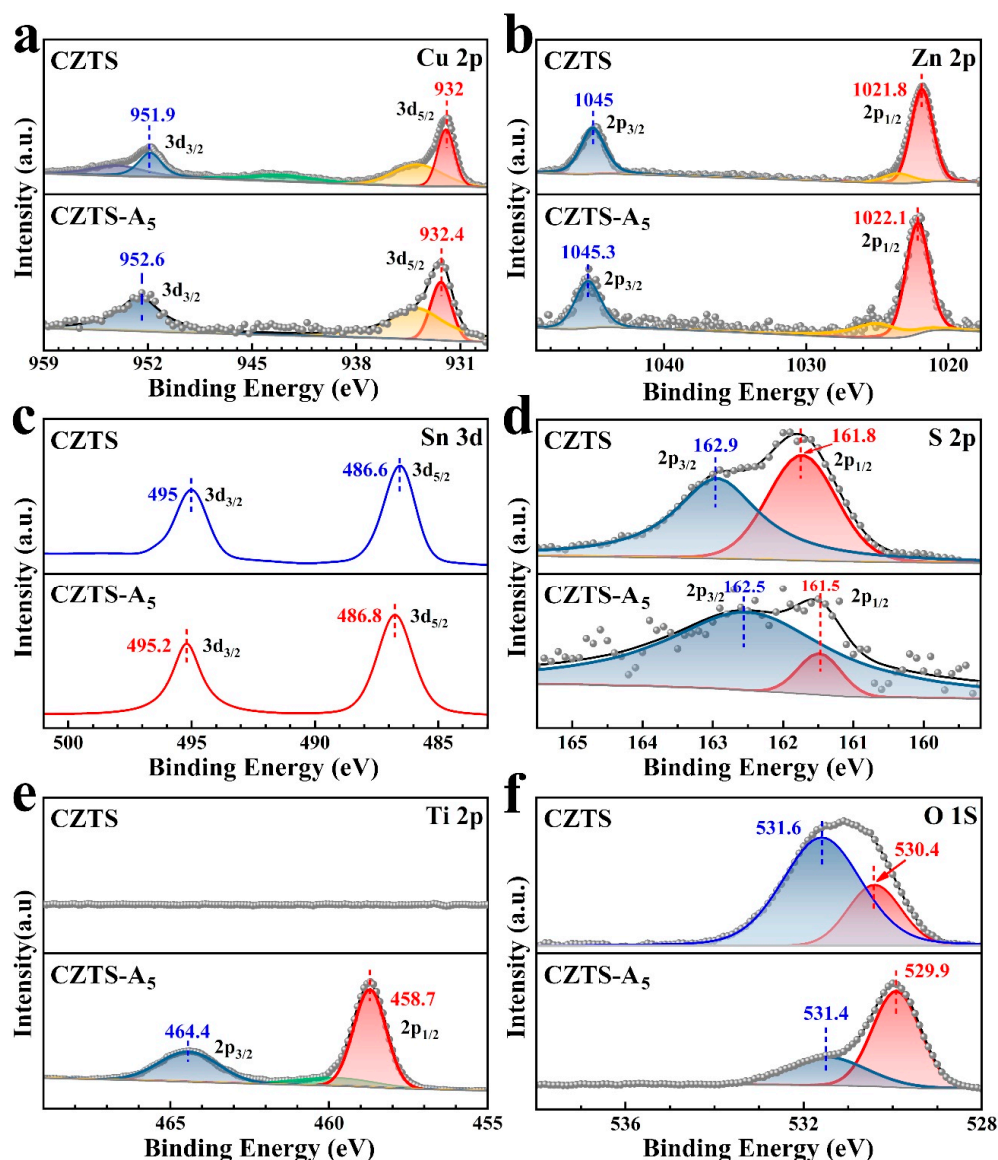

Figure 4. XPS spectra of the CZTS NPs and the CZTS–A_5 nanocomposites, which involve (**a**) Cu 3d, (**b**) Zn 2p, (**c**) Sn 3d, (**d**) S 2p, (**e**) Ti 2p, and (**f**) O 1s.

2.3. FTIR Characterization and Optical Characterization

Figure 5a presents the Fourier transform infrared spectra of functional groups in CZTS samples with different doping concentrations of titanium oxides (anatase). The spectra exhibit a broad feature within the range of 3100–3500 cm^{-1}, which can be attributed to the typical characteristics of physically adsorbed water and the stretching vibration of thiourea (~3400 cm^{-1}) [14,37,38]. In addition, as the concentration of titanium dioxide increases, broad absorption peaks corresponding to the stretching vibration modes of Ti-O and Ti-O-Ti groups appear in the 400–700 cm^{-1} region, and these modes increase with the increase in concentration. Moreover, the main peaks corresponding to the metal–thiourea complex are

also observed at around 1100 cm^{-1}, 1400 cm^{-1}, and ~1650 cm^{-1} [14,39,40]. These values largely coincide with those reported in the research papers, but slight deviations exist. The ultraviolet–visible absorption properties of TiO$_2$ (anatase), CZTS NPs, and the mixed CZTS–A$_5$ nanocomposite were investigated using a UV–Vis spectrometer, as shown in Figure 5b. The UV–Vis absorption spectra from CZTS NPs recorded within the wavelength range of 200–800 nm show a significant response throughout the visible spectrum, while TiO$_2$ (anatase) NPs show a response only below 390 nm [14,37,38]. Furthermore, the absorption of the CZTS–A$_5$ nanocomposite sample is enhanced within the wavelength range of 350–800 nm compared to TiO$_2$ (anatase), indicating a complementary relationship between the synthesized CZTS and TiO$_2$, which correspond to their narrow band gap (1.5 eV) and wide band gap (3.2 eV), respectively [14,16].
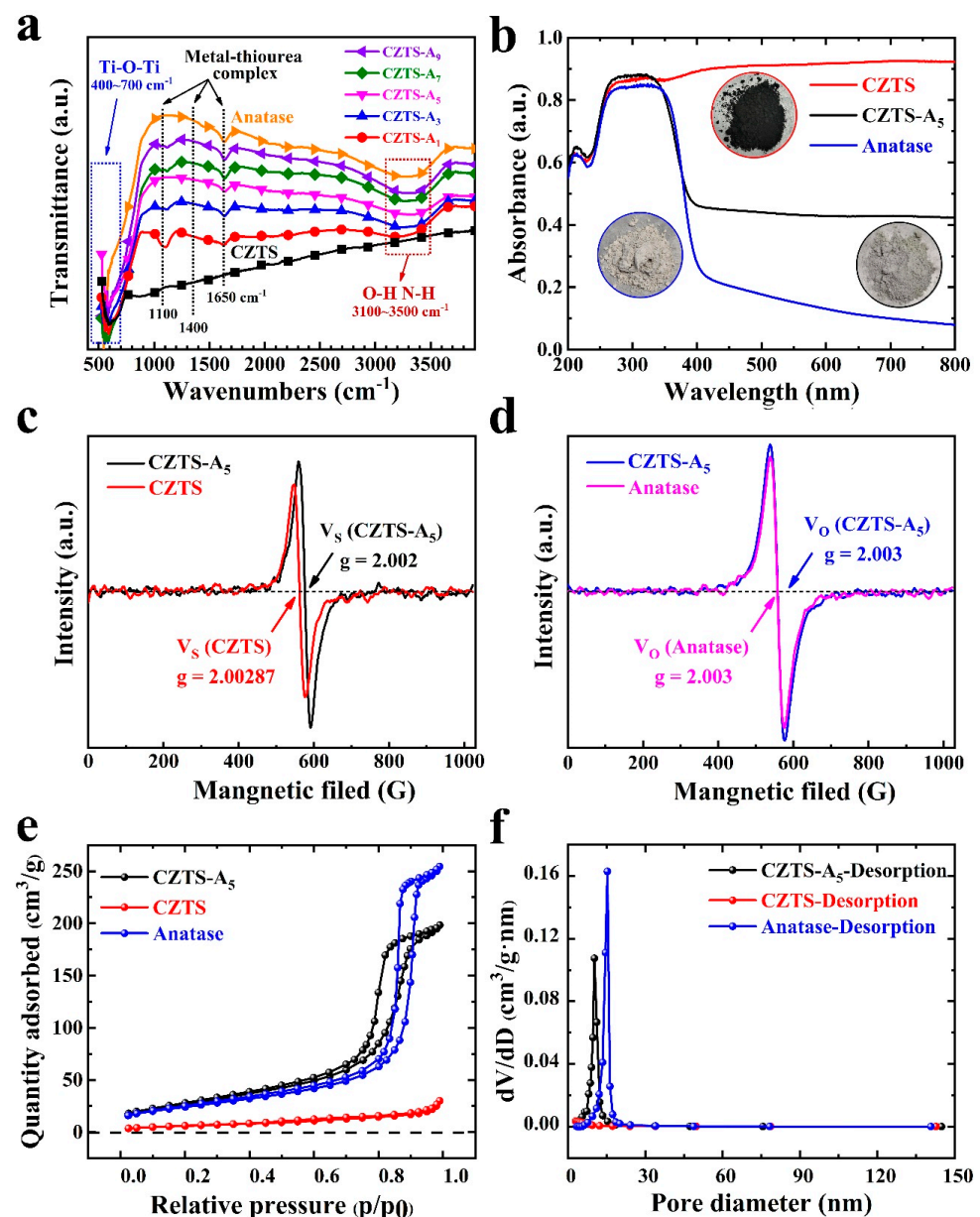

Figure 5. CZTS, TiO$_2$ (anatase), and CZTS–A$_X$ (X = 1, 3, 5, 7, 9) nanocomposites of FTIR spectra (**a**), CZTS, TiO$_2$ (anatase), and CZTS–A$_5$ nanocomposites of (**b**) UV–Vis analysis, (**c,d**) EPR spectra of CZTS NPs, TiO$_2$ (anatase) NPs, and hybrid CZTS–A$_5$ nanocomposites recorded at room temperature. (**e,f**) N$_2$ adsorption–desorption isotherms of CZTS NPs, hybrid CZTS–A$_5$ nanocomposites, and TiO$_2$ (anatase).

The band gap energy (E_g) can be determined by analyzing UV–visible diffuse reflectance spectroscopy (UV–Vis-DRS) data, specifically utilizing the Tauc plot. The formula for calculating E_g is as follows:

$$\alpha h v = \text{A} \times \left(h v - E_g \right)^{\frac{1}{2}} \tag{2}$$

In Equation (2), which illustrates the Tauc plot, α signifies the direct light absorption coefficient, h is Planck's constant, v represents the frequency of incident light, A is a proportionality constant, and E_g denotes the band gap energy of the semiconductor photocatalyst [35]. The band gap can be estimated based on the Tauc plot (Equation (3)). Consequently, from the test results of UV–visible diffuse reflectance spectroscopy, the band gaps of CZTS, TiO$_2$, and CZTS–A$_5$ can be inferred to be 1.25, 3.20, and 2.60 eV, respectively (as shown in Figure S4).

Conversely, the hybrid sample CZTS–A$_5$ exhibits weaker light absorption compared to CZTS, and its absorption in the visible light region is better than that of TiO$_2$ (anatase), indicating the formation of a heterojunction between TiO$_2$ (anatase) and CZTS, which covers the entire visible light spectrum. The HRTEM images reveal a good interface combination between TiO$_2$ and CZTS, suggesting that a heterojunction can evoke a sufficiently strong electric field, promoting photo-induced charge separation/transfer.

2.4. EPR Characterization

As shown in Figure 5c,d, further confirmation of sulfur/oxygen vacancies (in CZTS and CZTS–A$_5$) is provided by electron paramagnetic resonance (EPR) spectroscopy. Due to the abundance of unpaired electrons in materials possessing vacancy defects, Electron Paramagnetic Resonance (EPR) is commonly used to identify these unpaired electrons within the material. This, in turn, facilitates the recognition and quantification of vacancies through EPR analysis [41].

From Figure 5c, a signal located at g = 2.00287 and g = 2.002 is detected in CZTS and CZTS–A$_5$, respectively, which is attributed to the F center, i.e., a sulfur vacancy carrying a single negative charge [36,41], confirming the presence of sulfur vacancies in CZTS and CZTS–A$_5$ prepared using this method.

Additionally, the comparison with Figure 5d reveals that adding TiO$_2$ (anatase) leads to the formation of oxygen vacancies in CZTS–A$_5$, as indicated by the detection of a signal at g = 2.003, which is precisely the same as that signal from the pure anatase TiO$_2$. Upon comparing the peak intensities of CZTS–A$_5$ and TiO$_2$, a marginal amplification was detected in CZTS–A$_5$ relative to TiO$_2$. Such an observation can be explained by the augmented number of oxygen vacancies arising from the composition of the hybrid material [42]. This boost possibly originates from the synergistic effect between CZTS–A$_5$ and TiO$_2$, which presumably catalyzes the creation of oxygen vacancies.

By comparing the peak intensity of sulfur vacancies and oxygen vacancies, it can be deduced that the doping of TiO$_2$ (anatase) forms heterojunctions with CZTS, leading to the generation of more defects and, consequently, more vacancies. Oxygen vacancies can reshape the electronic configuration on the material's exterior, thereby facilitating meticulous manipulation of the density of active electrons and significantly adjusting the semiconductor's band gap. Furthermore, sulfur (S) vacancies can reduce the energy required for hydrogen adsorption [37,40]. As a result, the proliferation of these vacancies plays a favorable role in augmenting the catalytic proficiency of the CZTS-TiO$_2$ (anatase) heterojunction.

2.5. BET Characterization

To investigate the influence of the composite on the structure of the composite material among semiconductors, the specific surface area and porosity of the catalyst were comparatively analyzed. The Brunauer-Emmett-Teller (BET) structural properties of Cu$_2$ZnSnS$_4$ (CZTS), TiO$_2$ (anatase), and mixed CZTS–A$_X$ (X = 3, 5, 9) nanocomposites were primarily determined via the nitrogen adsorption–desorption isotherm.

As shown in Figure 5e,f, the samples belong to the mesoporous structure, and the isotherms of all the comparative samples exhibit a hysteresis loop characteristic of type IV behavior. As shown in Table 1, the measured BET-specific surface areas are as follows: TiO_2 (anatase) (87.223 m^2g^{-1}), Cu_2ZnSnS_4 (CZTS) (22.022 m^2g^{-1}), and mixed CZTS–A_X (X = 3, 5, and 9) (132.280, 98.954, and 126.612 $m^2\ g^{-1}$). Therefore, the hybrid nanocomposites have significantly higher specific surface areas compared to pure TiO_2 (anatase) and Cu_2ZnSnS_4 oxides. Notably, CZTS–A_5 has the smallest average particle size, indicating a better performance due to increased contact with the sacrificial agent. From Figure S6, we can see that the pore size of CZTS–A_5 is a bit larger compared to CZTS–A_3, and it can be considered that its particle size is smaller, but its stacked-up pore size becomes larger, so it leads to a smaller specific surface area. In addition, the addition of TBOT also shows the ability to modulate the textural properties of the sample, such as specific surface area and porosity.

Table 1. Comparison of different pore size distributions of BET in CZTS NPs, TiO_2 (anatase) NPs, and hybrid CZTS–A_X (X = 3, 5, 9) nanocomposites.

Samples	S_{BET} ($m^2\ g^{-1}$)	Pore Volume ($cm^3\ g^{-1}$)	Average Pore Size (nm)	Most Frequent Pore Diameter (nm)
anatase	87.223	0.372	1.805	–
CZTS	22.022	0.042	8.488	–
CZTS–A_3	132.280	0.301	9.101	8.743
CZTS–A_5	98.954	0.312	1.239	10.300
CZTS–A_9	126.612	0.306	9.562	8.739

2.6. Electrochemical (EC), Photoelectrochemical (PEC) and Photocatalytic (PC) Performance

This study evaluated the photocatalytic hydrogen production performance of CZTS NPs, TiO_2 (anatase) NPs, and CZTS–A_X (X = 1, 3, 5, 7, and 9) nanocomposites. The results are shown in Figure 6a,b.

Figure 6a,b shows that the hydrogen production of pure TiO_2 (anatase) and CZTS NPs is deficient, which can be attributed to the high recombination rate of photo-generated electrons/holes. Compared with pure TiO_2 (anatase) and CZTS NPs, the hydrogen production of hybrid CZTS–A_5 increased by about 11 times (0.0465 vs. 0.5017 mmol/g/h, CZTS–A_5 vs. TiO_2 anatase) and about 250 times (0.002 vs. 0.5017 mmol/g/h), respectively. The results indicate that the p-n heterojunctions formed by combining CZTS and TiO_2 (anatase) promote effective charge transfer and separation between interfaces, reducing the recombination rate of photo-generated electrons/holes.

In addition, as shown in Figure 6c, in order to further understand the comparison of the photocatalytic hydrogen production performance of anatase, CZTS, and composite materials, we compared the photocatalytic performance of anatase, CZTS, and composite CZTS–A_5 samples. It can be seen that compared with single CZTS and anatase, the composite CZTS–A_5 can produce hydrogen at a rate of 0.613 mmol/g/h, while CZTS and anatase produce only 0.005 mmol/g/h and 0.047 mmol/g/h. As shown in Figure 6b, the CZTS–A_5 sample, which has a 5 mL TBOT addition, exhibits the best photocatalytic H_2 generation performance. To investigate the stability of photocatalysts, we centrifuged the CZTS–A_5 sample from the electrolyte after ten hours of photocatalysis, refreshed the sacrificial agent, and subjected it to four light cycles. The obtained data are almost unchanged, as shown in Figure 6d.

Further research evaluated the photoelectrochemical (PEC) performance of the as-prepared CZTS–A_X samples with different concentrations of TBOT content. Figure 6e shows the linear sweep voltammetry (LSV) curves of the CZTS, CZTS–A_5, and TiO_2 (anatases) photoanodes under the AM 1.5G light irradiation.
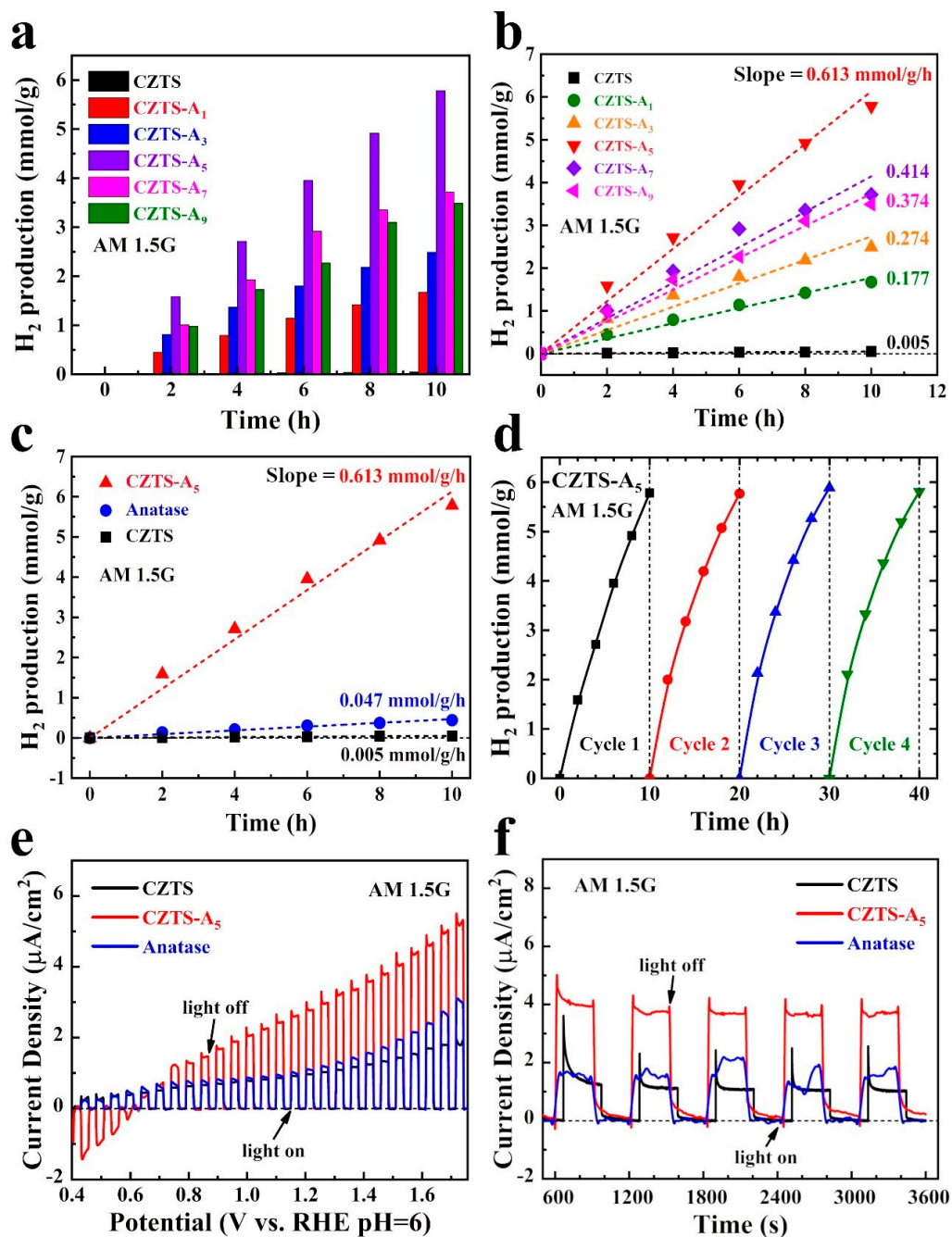
Figure 6. (**a**,**b**) CZTS NPs, hybrid CZTS–A_5 nanocomposites, and TiO_2 (anatase) photocatalyzes the water–splitting H_2 generation for 10 h using ethanol as a sacrificial agent under full spectrum light (the slopes associated with the hydrogen reaction rate simulations are 0.613, 0.414, 0.374, 0.274, and 0.177 mmol/g/h, respectively); (**c**) The photocatalytic activity of CZTS, CZTS–A_5, and TiO_2 (anatase) with the existence of ethanol as a sacrificial agent for 10 h; (**d**) Cyclic test of H_2 generation in CZTS–A_5 samples under full spectrum light irradiation; (**e**) Chopped linear sweep voltammetry (LSV) curve; and (**f**) chrono amperometry data plot of CZTS, CZTS–A_5, and TiO_2 (anatase) samples observed under the bias voltage of 1.5V (vs. RHE, the electrolyte is 0.5 M Na_2SO_4, pH = 6).

The photocurrent density of the CZTS–A_5 sample is 2.81 µA cm^{-2} at 1.23 V relative to RHE, which is 2.6 times that of TiO_2 (1.08 µA cm^{-2}) and about 3 times that of the original CZTS (0.93 µA cm^{-2}). The improvement in photoelectric performance can be attributed to the forming of a p/n junction, which enhances the charge separation mechanism, resulting in a strong photocurrent response in CZTS–A_5; however, as illustrated in Figure S5, the

light-induced current behavior in the mixed nanocomposites with a higher TiO_2 content (such as CZTS–A_7 and CZTS–A_9) has decreased, which is due to the dominance of the TiO_2 (anatase) content, resulting in the formation of a composite center, thereby accelerating the electron–hole recombination, see Figure S5.

We further explored the stability of the photoanode under different specific bias voltages. Typically, the chronoamperometry measurements were conducted at 1.5 V. (vs. RHE pH = 6) to verify the stability of the catalyst, as shown in Figure 6f. Compared to CZTS and TiO_2, CZTS–A_5 exhibits the highest photocurrent density, as shown in LSV. Additionally, in terms of stability, the CZTS–A_5 sample exhibits a higher stability over extended cycles compared to TiO_2, indicating a significant improvement in photostability.

Before conducting the addition bias test on the catalyst, we employed the electrochemical noise (ECN) mode to measure the photocurrent density of the sample without any bias voltage and before any damage to the catalyst's performance for performance evaluation. This non-destructive and in situ monitoring technology can study the self-generated chemical reactions on photoanodes (Figure 7a,c).
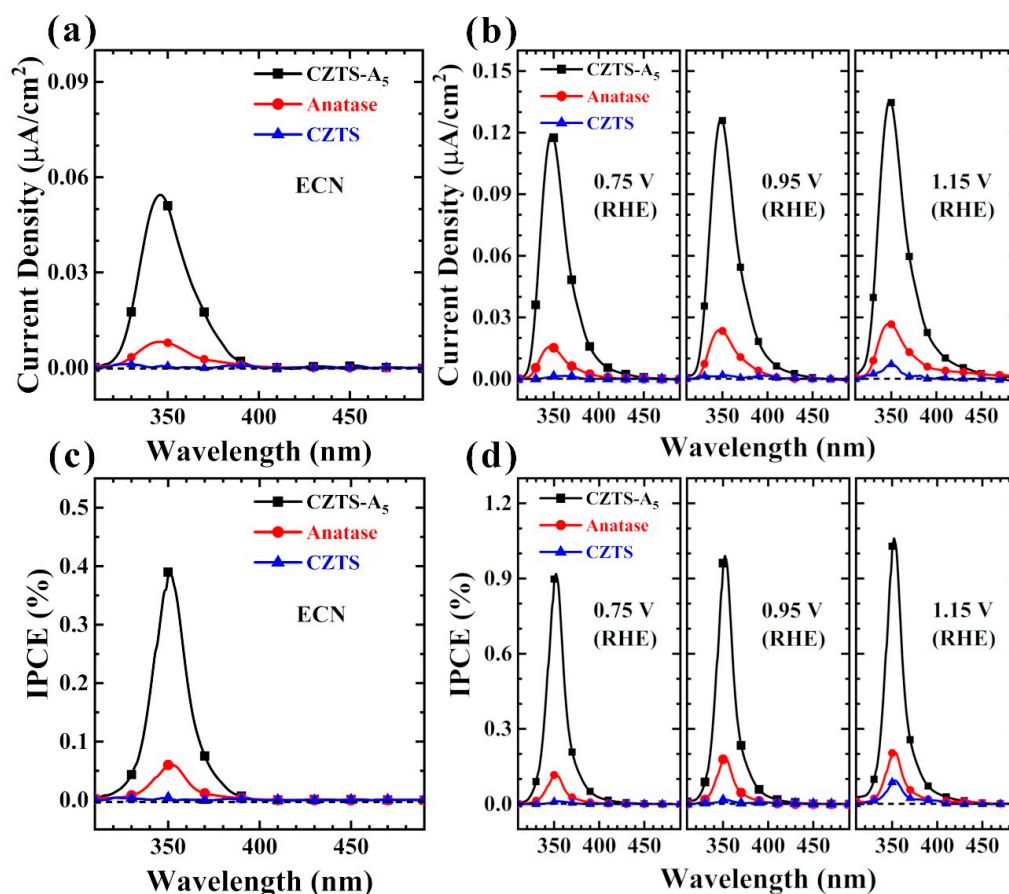

Figure 7. Relationship between photocurrent density and monochromatic light in electrochemical noise (ECN) mode (**a**) and photocurrent density and monochromatic light to generate IPCE (%) spectra (**b**); spectra of the relationship between photocurrent density and IPCE (%) spectra evaluated at different wavelengths of monochromatic light by applying different bias voltages (**c,d**) (electrolyte is 0.5 M Na_2SO_4, pH = 6).

Based on the data of hydrogen production and LSV measurements, further studies were only conducted on CZTS, TiO_2 (anatase), and CZTS–A5 in the following measurements. To further explore the influence of the light absorption range of the photoanode, we performed IPCE testing on the photoanode.

As shown in Figure 7, the luminous flux density of CZTS–A_5 is higher than that of CZTS and TiO_2 (anatase). Figure 7d shows the monochromatic radiation characteristics of

CZTS, TiO$_2$ (anatase), and CZTS–A$_5$ at different bias voltages. The IPCE value of CZTS–A$_5$ is the highest at a wavelength of 358 nm, reaching 1.08%. Compared with CZTS and TiO$_2$, the IPCE values have significantly increased 10 times (1.08% vs. 0.10%) and 5 times (1.08% vs. 0.20%), respectively, indicating that CZTS–A$_5$ responds significantly to light. The photocurrent response of CZTS–A$_5$ increases with the increase in the bias voltage, and the same phenomenon is shown in the linear sweep voltammetry (LSV) curve results. Similarly, the data demonstrate that CZTS–A$_5$ has improved visible light absorption, mainly distributed below 480 nm, while the two undoped comparative samples of CZTS and TiO$_2$ (anatase) do not show this improvement.

The band gap (E_g) of CZTS, CZTS–A$_5$, and TiO$_2$ (anatase) can be obtained from the IPCE spectra, as shown in Figure 8a, with values of 2.07 eV, 2.50 eV, and 3.20 eV, respectively. Thus, the band structure of the samples can be determined. To further verify the photoinduced e$^-$/h$^+$ separation, electrochemical impedance spectroscopy (EIS) was applied to the analysis of TiO$_2$ (anatase), CZTS NPs, and CZTS nanocomposites (Figure 8b and Table S1). Typically, we believe that the radius of the arc is proportional to the electrochemical reaction rate of the catalyst on the electrode surface. The EIS diagram with the smallest arc radius has the highest electrochemical reaction rate, implying that it has the fastest interface charge transfer and the highest photoinduced e$^-$/h$^+$ separation efficiency. Compared with the mixed nanocomposites, the arc radius of TiO$_2$ (anatase) is the largest, and its electrochemical reaction rate is the lowest. The samples CZTS and CZTS–A$_5$ show Nyquist curves with gradually decreasing arc radii, indicating a higher efficiency of photoinduced e$^-$/h$^+$ separation. The arc radius of CZTS–A$_5$ is the smallest, and the efficiency of photoinduced e$^-$/h$^+$ separation is the highest. Therefore, the EIS results confirm the results of the photocurrent response.
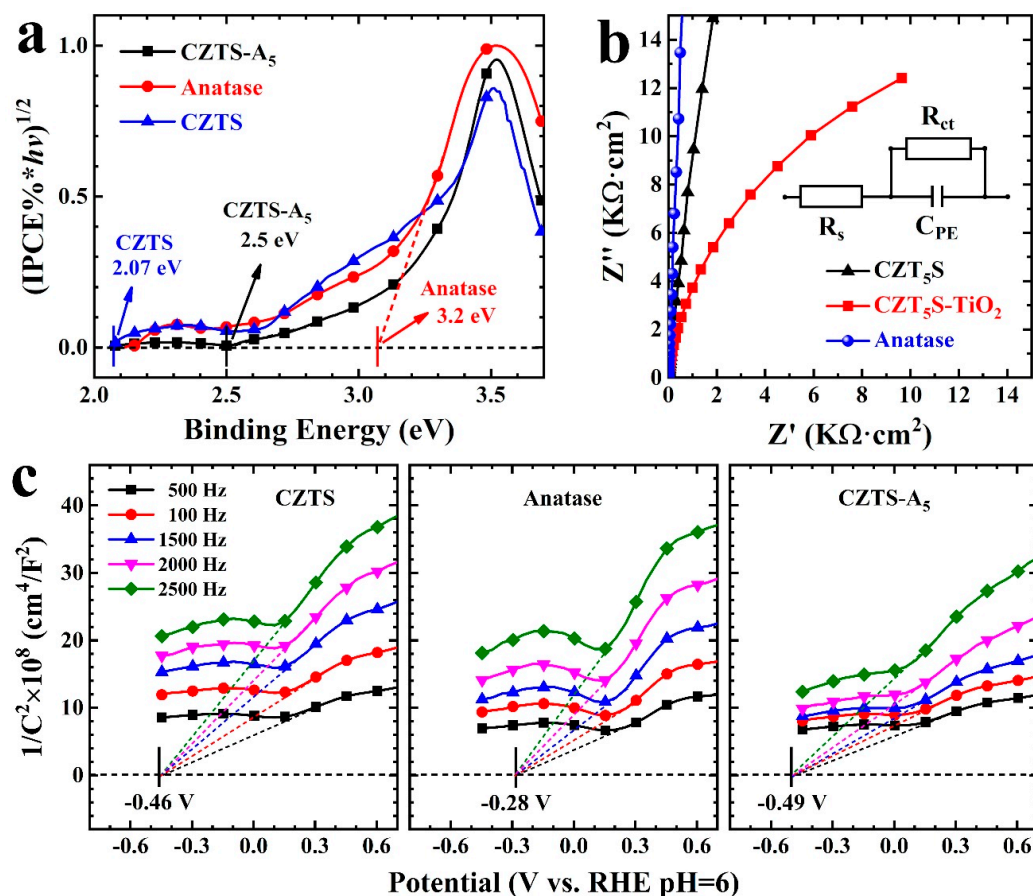

Figure 8. (**a**) Band gap plot determined by examining the relationship between (IPCE% $\times$ hv)$^{1/2}$ and photon energy (hv); (**b**) EIS impedance plot; (**c**) Mott–Schottky plot.

In addition, the band structure of the prepared samples was also studied using the Mott–Schottky measurement method. The calculated flat-band potentials of CZTS, TiO_2 (anatase), and CZTS–A_5 are −0.46 V, −0.28 V, and −0.49 V, respectively. Compared with CZTS and TiO_2, the flat-band potential of CZTS–A_5 moves more negatively (Figure 8c).

In hydrogen production by the photocatalytic water decomposition catalyst, we propose a p-n heterojunctions mechanism, which is supported in subsequent experiments (see Figure 9). The significant improvement in photocatalytic hydrogen production efficiency is attributed to the strong enough built-in electric field formed by heterojunctions, which improves the efficiency of photo-generated charge carriers separation/transfer and enhances the production rate of photocatalytic H_2 production. When CZTS–A_5 is illuminated, electrons migrate from the conduction band (CB) of anatase titanium dioxide (TiO_2) to the valence band (VB) of CZTS. Then, they are excited to the CB of CZTS, resulting in charge separation. The sulfur and oxygen vacancies generated in the CZTS–TiO_2 hybrid nanocomposite facilitate the rapid migration of electrons and increase the photocatalytic activity. When electrons and holes are separated, they migrate towards CZTS and TiO_2, respectively, which inhibits electron-hole recombination. In the whole mechanism of photocatalytic H_2 generation, the oxidation reaction is driven by the holes in the VB of CZTS, and the holes consume ethanol to generate H^+ ions and O_2, which makes it easier to react with H^+ ions, thereby increasing the generation rate of H_2.
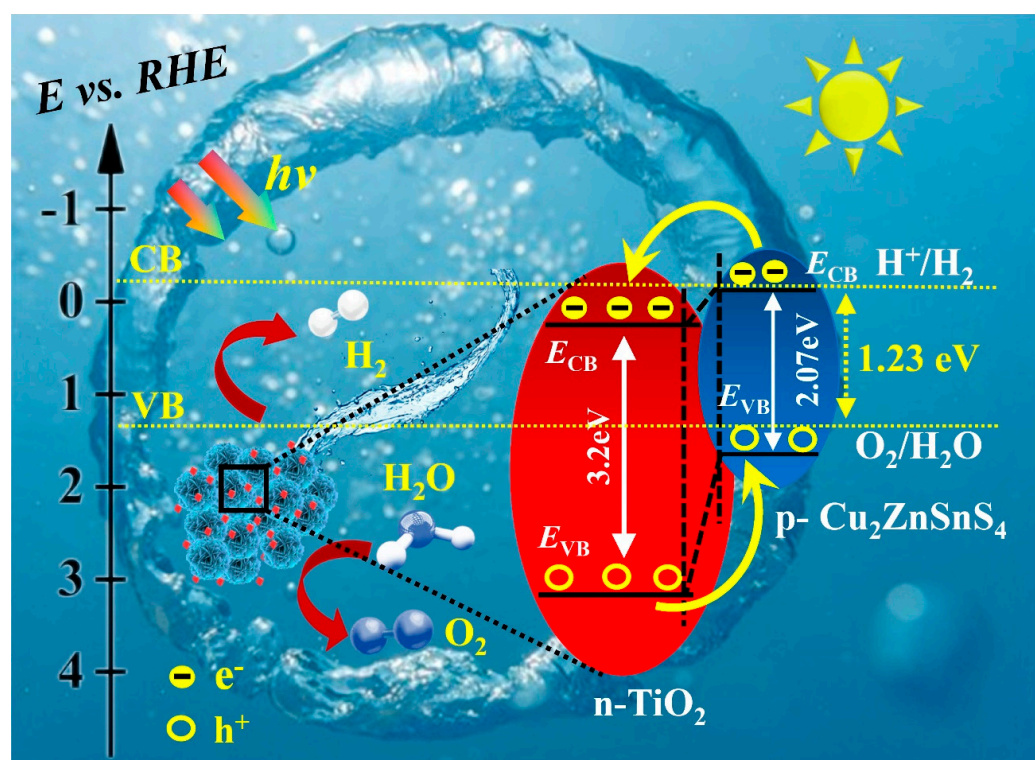

Figure 9. Proposed band gap structure diagram of the Cu_2SnZnS_4–TiO_2 (anatase) hybrid nanocomposites.

3. Materials and Methods

3.1. Materials

All the chemicals and reagents applied in this study were of analytical grade. $CuCl_2 \cdot 2H_2O$ (99%), Zn $(CH_3OO)_2 \cdot 2H_2O$ (99%), $SnCl_2$ (99%), thiourea (NH_2CSNH_2) (99%), anhydrous ethanol (C_2H_6O, AR), and tetra-n-butyl titanate (TBOT, $C_{16}H_{36}O_4Ti$) were obtained from General-Reagent, Sinopharm Chemical Reagent Co., Ltd., Shanghai, China. All experiments were conducted using deionized water.

3.2. Synthesis Method

In the first step of the experiment, $CuCl_2 \cdot 2H_2O$, $Zn(CH_3OO)_2 \cdot 2H_2O$, $SnCl_2$, and thiourea in the ratio of (2:1:1:8), all with an average dosage of 1 mmol, were dissolved in a beaker containing a mixture of ultrapure water and anhydrous ethanol in a ratio of 1:1. The mixture was sonicated for 30 min at room temperature. After thorough stirring, tetra-n-butyl titanate ($C_{16}H_{36}O_4Ti$, TBOT) was added dropwise in different ratios (0, 1, 3, 5, 7, 9 mL), and the mixture was sonicated for 1 h. The resulting suspension was transferred to a stainless-steel autoclave and heated at 200 °C for 24 h in an oven. The solution was then cooled, centrifuged, and washed repeatedly with deionized water and ethanol. The resulting black powder was homogenized and annealed at 400 °C under an argon atmosphere in a tube furnace for 2 h. The final sample was obtained after natural cooling. The experimental procedure is shown in Figure 10, and the final samples were denoted as CZTS–A_x, where X = 0, 1, 3, 5, 7, or 9 mL of TBOT. Moreover, to evaluate whether the PC/PEC performances of the CZTS–A_x heterojunction hybrid nanocomposite were improved, pure Cu_2ZnSnS_4 (CZTS) NPs and pure TiO_2 (anatase) NPs were prepared through a similar synthesis scheme.
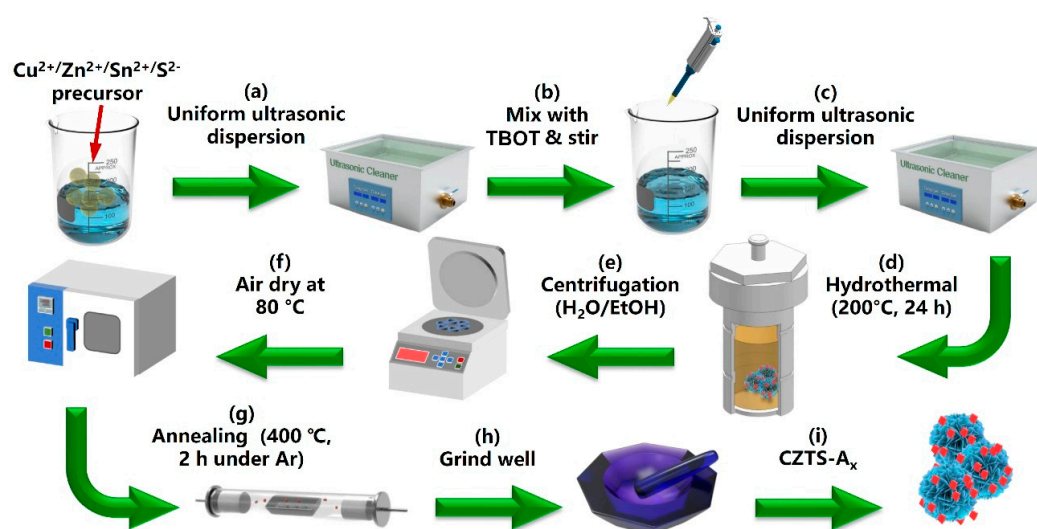

Figure 10. Schematic illustration for the fabrication strategy of the CZTS and the CZTS–A_x nanocomposite.

3.3. Characterization

The crystal structure and phase of the composite materials were determined by X-ray diffraction using a X-ray diffractometer (Cu Kα1 1.5418 Å, 40 kV, 100 mA, measurement range of 20–80°, XRD, Rigaku D/max-2400, Akishima, Rigaku, Tokyo, Japan). Scanning electron microscopy equipped with energy dispersive spectroscopy (SEM, Apreo SLoVac, CZ, Thermo Fisher, Waltham, MA, USA) and high-resolution transmission electron microscopy (FEI-TALOS-F200X, Hillsboro, OR, USA) were used for the morphological analysis of the samples (TEM, HRTEM, SAED, Thermo Fisher Scientific, Waltham, MA, USA). Elemental stoichiometry was determined using an energy dispersive spectrometer (EDS) installed on the SEM (EDS, Apreo SLoVac, CZ, Thermo Fisher, Waltham, MA, USA). To evaluate surface functional groups, a Nicolet iS 50 Fourier transform infrared spectrometer (FT-IR, Thermo Fisher, Waltham, MA, USA) was used to perform Fourier-transform infrared spectroscopy (FT-IR) in the range of 400–4000 cm^{-1} on KBr pellets.Utilized X-ray photoelectron spectroscopy (XPS) with a monochromatic Al-K-α (1486.6 eV) radiation source (XPS, Thermo Fisher Scientific K–Alpha, Waltham, MA, USA) to investigate the elemental composition and electronic valence states of the composite materials. The specific surface area and porosity of the samples were characterized and confirmed using the Brunauer-Emmett-Teller (BET) method with the V-Sorb 2800P instrument (BET, Gold APP Instruments Corp. LTD, Beijing, China). Ultraviolet/visible diffuse reflectance spectra (UV-

Vis) were recorded using a laboratory-equipped Cary 5000 spectrometer (UV-Vis, Agilent, Santa Clara, CA, USA), with $BaSO_4$ as the reference. Electron paramagnetic resonance (EPR) spectra at room temperature were recorded using a Bruker (Billerica, MA, USA) A300 spectrometer to determine the oxygen vacancies and sulfur vacancies in the composite materials, (EPR, Bruker Biospin GmbH, Rheinstetten, Germany).

3.4. Photoelectrochemical (PEC) Measurements

In a specially designed experimental reactor, each photocatalyst was mixed with ultrapure water and naphthol. Then, the mixture was ultrasonicated for 30 min to achieve uniform dispersion. A tin-doped indium oxide (FTO) glass with an active area of 1 square centimeter was used as the substrate. A 50 µL suspension was uniformly dropped on the FTO glass and spin-coated six times. Then, the sample was air-dried overnight. Photocurrent measurement was carried out under a standard three-electrode system, with the FTO glass loaded with the sample as the working electrode. The effective illuminated area was 1.0 square centimeter, and a platinum plate was used as the counter electrode. The reference electrode was a Ag/AgCl electrode, and the electrolyte solution was 0.5 mol L^{-1} Na_2SO_4. Under the irradiation of a high-uniformity integrated xenon light source (PLS-FX300HU, Beijing Perfect Light Source Company, Beijing, China) with AM 1.5G (100 mW cm^{-2}), the samples were measured using an electrochemical workstation (CHI760E) by linear sweep voltammetry (LSV) and chronoamperometry (I-t). During the linear sweep voltammetry (LSV) measurement, a shutter with a frequency of 5 s^{-1} was used to cut off the light. For the chronoamperometry (I-t) measurement, alternate illumination was cut off with a shutter of 300 s^{-1} and performed at a potential of 1.0 V (compared to RHE at pH = 6). The catalyst area of the working electrode was completely immersed in the electrolyte. By applying the Nernst equation to Equation (1), the measured potential was converted to the reversible hydrogen electrode (RHE) scale according to the Nernst equation (Equation (3)) [6,10,11,15,43–46]:

$$E_{RHE} = E_{Ag/AgCl} + 0.0592 \times pH + E^0_{Ag/AgCl} \tag{3}$$

where the $E^0_{Ag/AgCl}$ = 0.1976 V vs. Ag/AgCl at room temperature.

The incident photon-to-current efficiency (IPCE) was measured using a 300 W xenon lamp equipped with a grating monochromator (7ISU, SOFN Instruments Co., Ltd., Beijing, China) and a filter to eliminate higher-order diffraction. A potentiated instrument (CS350H, Wuhan KRITE Instrument Co., Ltd., Wuhan, China) was used to collect and process the signals and for electrochemical impedance spectroscopy (EIS) and Mott–Schottky (M-S) curve measurements.

The test setup included an electrochemical workstation (CS350H, CorrTest, Wuhan, China), a 300 W xenon light source (PLS-SXE300D, Perfect Light Source Co., Ltd., Beijing, China), and a grating monochromator (7ISU, SOFN Instruments Co., Ltd., Beijing, China). The grating monochromator was equipped with a filter to eliminate higher-order diffraction for measuring the incident photon-to-current efficiency (IPCE). The IPCE value was determined using the formula provided (Equation (4)) [6,10,11,15,43,45].

$$IPCE(\%) = \frac{1240 \times J_p}{\lambda \times I_0} \times 100\% \tag{4}$$

where IPCE represents the incident photon-to-current efficiency, λ represents the wavelength of the incident light, I_0 represents the photocurrent, and J_p represents the incident light intensity.

In the dark, electrochemical impedance spectroscopy (EIS) and Mott–Schottky (M-S) plots were measured using an electrochemical workstation (Squidstat Plus, IME, Tempe, AZ, USA). The working frequency range of the electrochemical analyzer is from 0.01 to 100,000 Hz, with a voltage increment of 0.005 V and an AC amplitude of 10 mV. In a typical

M-S measurement, the test frequencies of the working electrode are 500, 1000, 1500, 2000, and 2500 Hz, respectively [44,46–48].

3.5. Photocatalytic (PC) Hydrogen Evaluation

The MCP-WS1000 photochemical workstation, produced by Perfect Light Source Technology Co., Ltd., Beijing, China, includes a 50 mL quartz reactor to evaluate the photocatalytic (PC) hydrogen evolution. This device is employed to assess the performance of photocatalytic hydrogen production under full-spectrum light irradiation. In this configuration, the prepared photocatalyst is dispersed in a solution composed of anhydrous ethanol and an equal amount of ultrapure water by using ultrasound for 30 min. Before measuring the H_2 evolution, it is purged with argon for 10 min. A lamp array consisting of 9 full-spectrum lamps (10 W) provides visible light, and a water-cooling system is utilized to maintain the solution temperature at 5 °C during the photocatalytic reaction. The hydrogen evolution generated per hour is analyzed using a GC9790II gas chromatograph system produced by Zhejiang Fuli Analytical Instruments Inc., Wenling, China.

4. Conclusions

This study successfully synthesized a CZTS–TiO_2 (anatase) heterojunction nanocomposite using a one-step method, significantly enhancing the photocatalytic hydrogen production performance under solar irradiation. The nanocomposite's small particle size, large specific surface area, and high conductivity were critical factors in improving its performance. Notably, the H_2 yield of the CZTS–A_5 nanocomposite reached 0.5017 mmol/g/h, 250-times higher than that of the original CZTS. This remarkable increase can be attributed to the unique p-n heterojunctions formed between the CZTS photocatalyst and TiO_2 (anatase) loading. This structure benefits from the close interface contact between TiO_2 and CZTS, increasing sulfur vacancies at the interface, enhancing the photocatalytic activity, and providing numerous active sites for the H_2 generation reaction. Additionally, the earth-abundant nature of this nanocomposite's elements ensures good reproducibility and low cost, highlighting its potential for large-scale application in photocatalytic processes. The outcomes of this study pave the way for new methods of inefficient photocatalytic H_2 production and contribute to the advancement of sustainable solar technology for hydrogen fuel production.

Data Availability Statement: The original contributions presented in the study are included in the article/Supplementary Material, further inquiries can be directed to the corresponding author/s.

Conflicts of Interest: The authors declare no conflicts of interest.

References

1. Lu, Q.; Yu, Y.; Ma, Q.; Chen, B.; Zhang, H. 2D Transition-Metal-Dichalcogenide-Nanosheet-Based Composites for Photocatalytic and Electrocatalytic Hydrogen Evolution Reactions. *Adv. Mater.* **2016**, *28*, 1917–1933. [CrossRef]
2. Yokoyama, D.; Minegishi, T.; Jimbo, K.; Hisatomi, T.; Ma, G.; Katayama, M.; Kubota, J.; Katagiri, H.; Domen, K. H_2 Evolution from Water on Modified Cu_2ZnSnS_4 Photoelectrode under Solar Light. *Appl. Phys. Express* **2010**, *3*, 101202. [CrossRef]
3. Fujishima, A.; Honda, K. Electrochemical photolysis of water at a semiconductor electrode. *Nature* **1972**, *238*, 37–38. [CrossRef]
4. Jiang, C.; Moniz, S.J.A.; Wang, A.; Zhang, T.; Tang, J. Photoelectrochemical devices for solar water splitting-materials and challenges. *Chem. Soc. Rev.* **2017**, *46*, 4645–4660. [CrossRef] [PubMed]
5. Hisatomi, T.; Minegishi, T.; Domen, K. Kinetic Assessment and Numerical Modeling of Photocatalytic Water Splitting toward Efficient Solar Hydrogen Production. *Bull. Chem. Soc. Jpn.* **2012**, *85*, 647–655. [CrossRef]
6. Tong, M.-H.; Wang, T.-M.; Lin, S.-W.; Chen, R.; Jiang, X.; Chen, Y.-X.; Lu, C.-Z. Ultra-thin carbon doped TiO_2 nanotube arrays for enhanced visible-light photoelectrochemical water splitting. *Appl. Surf. Sci.* **2023**, *623*, 156980. [CrossRef]
7. Wang, J.; Ong, W.L.; Gao, M.; Zhu, L.; Ho, G.W. TiO_2-Based Heterogeneous Catalysis for Photocatalytic Hydrogen Generation and Photodegradation. In *Encyclopedia of Inorganic and Bioinorganic Chemistry*; John Wiley & Sons, Ltd.: Hoboken, NJ, USA, 2016; pp. 1–29. [CrossRef]
8. Efthimiopoulos, I.; Küllmey, T.; Speziale, S.; Pakhomova, A.S.; Quennet, M.; Paulus, B.; Ritscher, A.; Lerch, M.; Koch-Müller, M. Pressure-induced structural and electronic transitions in kesterite-type Cu_2ZnSnS_4. *J. Appl. Phys.* **2018**, *124*, 085905. [CrossRef]
9. Liao, M.; Wang, T.; Zuo, T.; Meng, L.; Yang, M.; Chen, Y.X.; Hu, T.; Xie, Y. Design and Solvothermal Synthesis of Polyoxometalate-Based Cu(II)-Pyrazolate Photocatalytic Compounds for Solar-Light-Driven Hydrogen Evolution. *Inorg. Chem.* **2021**, *60*, 13136–13149. [CrossRef] [PubMed]
10. Chen, R.; Wang, Y.; Jiang, X.; Ji, M.; Shi, H.; Wang, H.; Chen, Y.; Lu, C. Scheme Z Pd-NPs Embedded in 3DOM-$LaCoO_3$-Dispersed pCN Heterojunction for Stimulating Visible Light-Catalyzed Solar H_2 Production. *ACS Appl. Energy Mater.* **2023**, *6*, 11288–11298. [CrossRef]
11. Lin, S.; Tong, M.; Chen, Y.; Chen, R.; Zhao, H.; Jiang, X.; Yang, K.; Lu, C. CeO_2/TiO_2 Heterojunction Nanotube Arrays for Highly Efficient Visible Light Photoelectrochemical Water Splitting. *ACS Appl. Energy Mater.* **2023**, *6*, 1093–1102. [CrossRef]
12. Yu, Y.; Dong, X.; Chen, P.; Geng, Q.; Wang, H.; Li, J.; Zhou, Y.; Dong, F. Synergistic Effect of Cu Single Atoms and Au-Cu Alloy Nanoparticles on TiO_2 for Efficient CO_2 Photoreduction. *ACS Nano* **2021**, *15*, 14453–14464. [CrossRef]
13. Sakar, M.; Mithun Prakash, R.; Do, T.O. Insights into the TiO_2-Based Photocatalytic Systems and Their Mechanisms. *Catalysts* **2019**, *9*, 680. [CrossRef]
14. Raza, A.; Shen, H.; Haidry, A.A.; Shahzad, M.K.; Sun, L. Facile in-situ fabrication of TiO_2-Cu_2ZnSnS_4 hybrid nanocomposites and their photoreduction of CO_2 to CO/CH_4 generation. *Appl. Surf. Sci.* **2020**, *529*, 147005. [CrossRef]
15. Shi, W.; Cao, L.; Shi, Y.; Zhong, W.; Chen, Z.; Wei, Y.; Guo, F.; Chen, L.; Du, X. Boosted built-in electric field and active sites based on Ni-doped heptazine/triazine crystalline carbon nitride for achieving high-efficient photocatalytic H_2 evolution. *J. Mol. Struct.* **2023**, *1280*, 135076. [CrossRef]
16. Zhang, X.; Han, M.; Zeng, Z.; Lin, H.Q. The instability of S vacancies in Cu_2ZnSnS_4. *RSC Adv.* **2016**, *6*, 15424–15429. [CrossRef]
17. Levcenko, S.; Hajdeu-Chicarosh, E.; Garcia-Llamas, E.; Caballero, R.; Serna, R.; Bodnar, I.V.; Victorov, I.A.; Guc, M.; Merino, J.M.; Pérez-Rodriguez, A.; et al. Spectroscopic ellipsometry study of Cu_2ZnSnS_4 bulk poly-crystals. *Appl. Phys. Lett.* **2018**, *112*, 161901. [CrossRef]
18. Zhang, R.; Wen, X.; Xu, F.; Zhang, Q.; Sun, L. A Density Functional Theory Study of the Cu_2ZnSnS_4 Monolayer as a Photo-electrointegrated Catalyst for Water Splitting and Hydrogen Evolution. *J. Phys. Chem. C* **2020**, *124*, 11922–11929. [CrossRef]
19. Kageshima, Y.; Shiga, S.; Ode, T.; Takagi, F.; Shiiba, H.; Htay, M.T.; Hashimoto, Y.; Teshima, K.; Domen, K.; Nishikiori, H. Photocatalytic and Photoelectrochemical Hydrogen Evolution from Water over $Cu_2Sn_xGe_{1-x}S_3$ Particles. *J. Am. Chem. Soc.* **2021**, *143*, 5698–5708. [CrossRef] [PubMed]
20. Mukherjee, B.; Isotta, E.; Fanciulli, C.; Ataollahi, N.; Scardi, P. Topological Anderson Insulator in Cation-Disordered Cu_2ZnSnS_4. *Nanomaterials* **2021**, *11*, 2595. [CrossRef]
21. Zhu, X.; Xiong, J.; Wang, Z.; Chen, R.; Cheng, G.; Wu, Y. Metallic Copper Containing Composite Photocatalysts: Fundamental Materials Design and Photoredox Applications. *Small Methods* **2022**, *6*, 2101001. [CrossRef]
22. Chen, G.L.; Wang, W.H.; Lin, P.Y.; Cai, H.L.; Chen, B.W.; Huang, X.J.; Zhang, J.M.; Chen, S.Y.; Huang, Z.G. The effect of binary sulfides precursors with different value states on CZTS thin films. *Ceram. Int.* **2018**, *44*, 18408–18412. [CrossRef]
23. Semalti, P.; Sharma, V.; Sharma, S.N. A novel method of water remediation of organic pollutants and industrial wastes by solution-route processed CZTS nanocrystals. *J. Mater.* **2021**, *7*, 904–919. [CrossRef]
24. Chen, S.; Liu, T.; Zheng, Z.; Ishaq, M.; Liang, G.; Fan, P.; Chen, T.; Tang, J. Recent progress and perspectives on Sb_2Se_3-based photocathodes for solar hydrogen production via photoelectrochemical water splitting. *J. Energy Chem.* **2022**, *67*, 508–523. [CrossRef]

25. Chen, S.; Liu, T.; Chen, M.; Ishaq, M.; Tang, R.; Zheng, Z.; Su, Z.; Li, X.; Qiao, X.; Fan, P.; et al. Crystal growth promotion and interface optimization enable highly efficient Sb_2Se_3 photocathodes for solar hydrogen evolution. *Nano Energy* **2022**, *99*, 107417. [CrossRef]

26. Dursun, S.; Sarıipek, F.B.; Kılıç, S.; Gezgin, S.Y.; Gündoğdu, Y.; Kılıç, H.Ş. Investigation of photocatalytic activity (under visible light) of ultrathin CZTS films produced in different thicknesses by PLD method. *Opt. Quantum Electron.* **2023**, *55*, 166. [CrossRef]

27. Liang, G.; Li, Z.; Ishaq, M.; Zheng, Z.; Su, Z.; Ma, H.; Zhang, X.; Fan, P.; Chen, S. Charge Separation Enhancement Enables Record Photocurrent Density in $Cu_2ZnSn(S,Se)_4$ Photocathodes for Efficient Solar Hydrogen Production. *Adv. Energy Mater.* **2023**, *13*, 2300215. [CrossRef]

28. Ansari, M.Z.; Singh, S.; Khare, N. Visible light active CZTS sensitized CdS/TiO_2 tandem photoanode for highly efficient photoelectrochemical hydrogen generation. *Sol. Energy* **2019**, *181*, 37–42. [CrossRef]

29. Zhu, L.; Tao, J.; Tao, H.; Chen, S.; Shen, Y.; Xu, A.; Jiang, J.; Pan, L. In-situ growth of Cu_2ZnSnS_4 nanosheets on TiO_2 nanowires for enhanced photoelectrochemical performance. *J. Alloys Compd.* **2015**, *649*, 704–711. [CrossRef]

30. Efthimiopoulos, I.; Küllmey, T.; Speziale, S.; Pakhomova, A.S.; Quennet, M.; Paulus, B.; Ritscher, A.; Lerch, M. High-pressure behavior of disordered kesterite-type Cu_2ZnSnS_4. *Appl. Phys. A-Mater. Sci. Process.* **2021**, *127*, 616. [CrossRef]

31. Al-Ani, A.A.-S.; Tokay, B.; Zhu, W.; Chen, G.Z. Enhancement of photoconversion efficiency and light harvesting ability of TiO_2 nanotube-arrays with Cu_2ZnSnS_4. *Int. J. Hydrogen Energy* **2022**, *47*, 31003–31013. [CrossRef]

32. Yang, Z.; Zhu, Z.; Pan, X.; Ma, Z.; Zhang, X. Ultrafine Cu_2ZnSnS_4 quantum dots functionalized TiO_2 nanotube arrays for potential optoelectronic applications. *Ceram. Int.* **2020**, *46*, 2940–2948. [CrossRef]

33. Suryawanshi, M.P.; Ghorpade, U.V.; Shin, S.W.; Gang, M.G.; Wang, X.; Park, H.; Kang, S.H.; Kim, J.H. Enhanced Solar Water Oxidation Performance of TiO_2 via Band Edge Engineering: A Tale of Sulfur Doping and Earth-Abundant CZTS Nanoparticles Sensitization. *ACS Catal.* **2017**, *7*, 8077–8089. [CrossRef]

34. Sawant, J.P.; Kale, R.B. CZTS counter electrode in dye-sensitized solar cell: Enhancement in photo conversion efficiency with morphology of TiO_2 nanostructured thin films. *J. Solid State Electrochem.* **2019**, *24*, 461–472. [CrossRef]

35. Yang, Y.; Ding, Y.; Zhang, J.; Liang, N.; Long, L.; Liu, J. Insight into the Growth Mechanism of Mixed Phase CZTS and the Photocatalytic Performance. *Nanomaterials* **2022**, *12*, 1439. [CrossRef]

36. Xie, Q.; Wang, M.; Xu, Y.; Li, X.; Zhou, X.; Hong, L.; Jiang, L.; Lin, W.-F. S vacancy modulated $Zn_xCd_{1−x}S/CoP$ quantum dots for efficient H_2 evolution from water splitting under visible light. *J. Energy Chem.* **2021**, *61*, 210–218. [CrossRef]

37. Xin, X.; He, M.; Han, W.; Jung, J.; Lin, Z. Low-cost copper zinc tin sulfide counter electrodes for high-efficiency dye-sensitized solar cells. *Angew. Chem. Int. Ed.* **2011**, *50*, 11739–11742. [CrossRef]

38. Wang, K.; Zhang, L.; Su, Y.; Shao, D.; Zeng, S.; Wang, W. Photoreduction of carbon dioxide of atmospheric concentration to methane with water over CoAl-layered double hydroxide nanosheets. *J. Mater. Chem. A* **2018**, *6*, 8366–8373. [CrossRef]

39. Lin, S.J.; Ting, J.M.; Hsu, K.C.; Fu, Y.S. A Composite Photocatalyst Based on Hydrothermally-Synthesized Cu_2ZnSnS_4 Powders. *Materials* **2018**, *11*, 158. [CrossRef]

40. Wu, F.; Yang, R.; Lu, S.; Du, W.; Zhang, B.; Shi, Y. Unveiling Partial Transformation and Activity Origin of Sulfur Vacancies for Hydrogen Evolution. *ACS Energy Lett.* **2022**, *7*, 4198–4203. [CrossRef]

41. Yang, M.; Liu, J.; Xu, H.; Pei, Y.; Jiang, C.; He, D.; Xiao, X. Intrinsic defects of nonprecious metal electrocatalysts for energy conversion: Synthesis advanced characterization and fundamentals. *ChemPhysMater* **2022**, *1*, 155–182. [CrossRef]

42. Jin, J.; Wang, X.; Hu, Y.; Zhang, Z.; Liu, H.; Yin, J.; Xi, P. Precisely Control Relationship between Sulfur Vacancy and H Absorption for Boosting Hydrogen Evolution Reaction. *Nanomicro Lett.* **2024**, *16*, 63. [CrossRef]

43. Jiang, X.; Chen, Y.X.; Zhou, J.W.; Lin, S.W.; Lu, C.Z. Pollen Carbon Based Rare Earth Composite Material for Highly Efficient Photocatalytic Hydrogen Production from Ethanol Water Mixtures. *ACS Omega* **2022**, *7*, 30495–30503. [CrossRef]

44. Jian, J.; Kang, H.; Yu, D.; Qiao, X.; Liu, Y.; Li, Y.; Qin, W.; Wu, X. Bi-Functional Co/Al Modified $1T-MoS_2/rGO$ Catalyst for Enhanced Uranium Extraction and Hydrogen Evolution Reaction in Seawater. *Small* **2023**, *19*, 2207378. [CrossRef]

45. Li, H.; Xie, C.; Liao, Y.; Liu, Y.; Zou, Z.; Wu, J. Characterization of Incidental Photon-to-electron Conversion Efficiency (IPCE) of porous TiO_2/SnO_2 composite film. *J. Alloys Compd.* **2013**, *569*, 88–94. [CrossRef]

46. Wang, S.; Qiao, Y.; Liu, X.; Zhu, S.; Zheng, Y.; Jiang, H.; Zhang, Y.; Shen, J.; Li, Z.; Liang, Y.; et al. Reduced Graphene Oxides Modified Bi_2Te_3 Nanosheets for Rapid Photo-Thermoelectric Catalytic Therapy of Bacteria-Infected Wounds. *Adv. Funct. Mater.* **2022**, *33*, 2210098. [CrossRef]

47. Zhou, Y.; Ye, X.; Lin, D. Enhance photocatalytic hydrogen evolution by using alkaline pretreated corn stover as a sacrificial agent. *Int. J. Energy Res.* **2020**, *44*, 4616–4628. [CrossRef]

48. Mondal, S.; Das, S.R.; Sahoo, L.; Dutta, S.; Gautam, U.K. Light-Induced Hypoxia in Carbon Quantum Dots and Ultrahigh Photocatalytic Efficiency. *J. Am. Chem. Soc.* **2022**, *144*, 2580–2589. [CrossRef]